

Supplementary material for: An ice-sheet wide framework for englacial attenuation and basal reflection from ice penetrating radar data

T. M. Jordan¹, J. L. Bamber¹, C. N. Williams¹, J. D. Paden², M. J. Siegert³,
P. Huybrechts⁴, O. Gagliardini⁵, and F. Gillet-Chaulet⁶

¹Bristol Glaciology Centre, School of Geographical Sciences, University of Bristol, Bristol, UK.

²Center for Remote Sensing of Ice-Sheets, University of Kansas, Lawrence, USA.

³Grantham Institute and Earth Science and Engineering, Imperial College, University of London, London, UK.

⁴Department of Geography, Vrije Universiteit Brussels, Brussels, Belgium.

⁵Le Laboratoire de Glaciologie et Géophysique de l'Environnement, University Grenoble Alpes, Grenoble, France.

⁶Le Laboratoire de Glaciologie et Géophysique de l'Environnement, Centre National de la Recherche Scientifique, Grenoble, France.

In this supplementary material we firstly discuss the temperature sensitivity of the algorithm sample region (Sect. S1), and the tuning of the sample region tolerance (Sect. S2), which both accompany Sect 2.5 in the main article. We then illustrate the ice-sheet wide properties of the algorithm using the SICOPOLIS temperature field as an input (Sect. S3), as was shown for the GISM temperature field in Sect. 3.1. The convergence of the attenuation solution in drainage basins other than the SE GrIS (Sect. 3.2 in the main article) is then discussed (Sect. S4). Finally, we provide evidence of algorithm repeatability for independently analysed field campaign data (Sect. S5), which expands upon Sect. 3.4 in the main article.

S1 Temperature sensitivity of the algorithm sample regions

10 Maps for the target window vectors, R_1 - R_4 , using the SICOPOLIS temperature field are shown in Fig. S1. These are equivalent to Fig. 6 in the main text for the GISM temperature field, and a target window vector difference plot for the two temperature fields is shown in Fig. S2. It is evident that both temperature fields share the same ice-sheet wide trend that the target window vectors are larger in the interior of the ice sheet. Generally, the GISM temperature field has larger window vectors than
15 SICOPOLIS toward the ice margins. An explanation for this trend is that the horizontal gradient in the absolute values $\langle B_\infty \rangle$ (which is approximately equivalent to depth-averaged temperature) are larger toward the margins for the SICOPOLIS temperature field (also refer to Fig. 3c. in main article). The target windows vectors are more sensitive to temperature field, (in terms of absolute differences in target window vector length), in the northern interior of the GrIS. This is thought to arise because

20 the ‘segment approximation’ that is used in the target windowing procedure becomes more sensitive
in colder ice, where there is a smaller horizontal gradient in $\langle B_\infty \rangle$. Future refinements to the
algorithm could therefore consider developing a more refined target windowing procedure for the
sample region in colder ice

S2 Tuning the tolerance of the algorithm sample region

25 A free parameter in our sample region windowing method is the RMS tolerance metric that is used to
define the target window vectors and boundaries, (Eq. (7)). If the RMS tolerance is too small, then the
ice thickness range is insufficient to discriminate an attenuation trend and the solution accuracy and
related coverage regions are reduced. This point is illustrated by a comparison of algorithm coverage
regions for RMS=1 dB km⁻¹ and RMS=0.5 dB km⁻¹ in Fig. S3. The lower coverage for RMS=0.5
30 dB km⁻¹ arises primarily due to lower $r_{[PC]}^2$ values. Additionally, due to the smaller sample region
windows for RMS=0.5 dB km⁻¹ less of the grid points meet the minimum threshold of 20 data
points.

As the RMS tolerance is increased, the sample regions will contain individual ice columns with
a greater range of depth-averaged attenuation rates. This is undesirable for a bed-returned power
35 attenuation algorithm, which either assumes: (i) local stationarity or, (ii) makes a local attenuation
correction. For algorithms that assume local stationarity, the degree of systematic underestimation
the attenuation rate (described in Sect. 2.6 and Fig. 7) is predicted to increase with window size/RMS
tolerance. For the local attenuation correction variant of the bed-returned power method described
here, the local attenuation correction, Eq. (11), increases with the RMS tolerance. It therefore follows
40 that greater RMS tolerance values are more susceptible to bias from the Arrhenius temperature
model input. Subsequently, we suggest that the desired level of solution accuracy should inform
the choice the RMS tolerance. As discussed in the main article, for basal melt discrimination the
desired attenuation loss accuracy is ~ 5 dB. If this is rescaled by ice thickness for a sample region
in the interior of the ice-sheet (mean ice thickness ~ 2500 m), this results in a desired attenuation
45 rate accuracy ~ 1 dB km⁻¹. This choice is consolidated by our estimates of attenuation rate solution
accuracy in Sect. 3.4, and Sect. S5 which are similar to the predicted range of values over which the
ice columns are sampled.

S3 Ice-sheet wide properties using the SICOPOLIS temperature field

The ice-sheet wide properties of the radar algorithm using the SICOPOLIS temperature field are
50 shown in Fig. S4, and are equivalent to Fig. 8 in the main article for GISM. The map for $r_{[PC]}^2$ for
SICOPOLIS is very similar to GISM, and supports the view that the algorithm has greater utility
for identifying an attenuation trend in regions of rougher basal topography and where the absolute
values of the attenuation rate are higher. The regions of high $r_{[R_\infty]}^2$ /low r_{ratio}^2 for the two temperature

fields are less well correlated. For the reasons discussed in Sect. 2.7 it is difficult to establish whether,
55 for either temperature field, the majority of these regions correspond to: (i) true variation in the basal
reflector with ice thickness, (ii) a strong bias in the ice-sheet model temperature field. However, for
regions where there is ice core temperature data available it is possible to predict which scenario is
more likely. Notably, for the region surrounding the NEEM and Camp Century ice cores in North
West Greenland, the GISM temperature field is very close to the core data (Fig. S5). This is therefore
60 suggestive that the regions of high $r^2_{[R_\infty]}$ in Fig. 8 correspond to a true variation in the basal reflector
with ice thickness.

As described in Sect. 2.6, a minimum of 20 IPR (along-track averaged) measurements within each
target window is set as a threshold for including a grid cell in the linear regression procedure. Due
to the generally smaller target window vectors for the SICOPOLIS temperature field toward the ice
65 margins, Fig. S2, there are more grid cells that fall below this threshold if this temperature field is
used as input. This effect is particularly apparent along the western ice margin where the maps for
SICOPOLIS input in Fig. S4 are non-continuous.

S4 Demonstration of solution convergence in other drainage basins

We observe qualitatively similar attenuation solution behavior in drainage basins 3,5,6 to that de-
70 scribed for drainage basin 4 in the main article. In all these basins we observe algorithm solution
convergence and an associated reduction in the solution bias from the Arrhenius model input. An
example of the attenuation rate solution differences for drainage basin 6 (the SW GrIS) is shown in
Fig. S6a, with the radar-inferred distribution being approximately normally distributed about zero,
($\mu \pm \sigma = -0.18 \pm 1.56 \text{ dB km}^{-1}$), and the Arrhenius model input having a mean systematic bias of
75 $\mu = -1.66 \text{ dB km}^{-1}$. In drainage basins 1,2,7,8 we do not observe analogous solution convergence,
(in the sense of normally distributed difference distribution for the radar-inferred values). We do,
however, typically see a reduction in the mean systematic bias of the attenuation rate solution, rel-
ative to the Arrhenius model input. For example, in drainage basin 8 (the NW GrIS), the Arrhenius
model mean attenuation rate bias is $\mu = -3.62 \text{ dB km}^{-1}$, whereas the radar-inferred value is $\mu = -2.62$
80 dB km^{-1} (Fig. S6b). An explanation for why we observe solution convergence in some basins but
not others is thought to relate to the temperature dependence of the target windows (Sect. S1), which
is generally higher in the northern interior. In turn, this results in different IPR data being sampled
for the different temperature field inputs.

S5 Repeatability and uncertainty for independently analysed field seasons

85 In Sect. 3.4. we proposed that the attenuation solution uncertainty can be measured by: (i) solution
variation for different input temperature fields, (ii) solution variation for independently analysed field
seasons (with a fixed temperature field input). Since, for equivalent algorithm settings, the solution

variation for different input temperature fields is slightly higher, we focused upon this in the main article as it gives a better overall indicator of solution uncertainty.

90 A full summary of attenuation rate solution variation for different field season pairs is shown in Table S1 and an example of the distributions and mutual coverage regions is shown in Fig. S7. The mutual coverage regions occur where there are regions of intersecting flight tracks (Fig. 1a). As these overlap regions are quite small, we considered the GrIS as a whole when measuring solution variation. The general relationship between solution variation (as measured by the standard deviation
95 of the solution difference distribution) and algorithm coverage (as measured by the frequency of grid cells that contain IPR data), is similar to the case for different input temperature fields. For $(\alpha, \beta) = (0.60, 0.80)$, the mean standard deviation aggregated over the different field season combinations is 1.29 dB km^{-1} . This supports the conclusion in the main paper that this algorithm quality setting represents sufficient accuracy for defining a coverage region for discrimination of basal melt from
100 the reflection values.

References

- Macgregor, J. A., Li, J., Paden, J. D., Catania, G. A., and Clow, G. D.: Radar attenuation and temperature within the Greenland Ice Sheet, *Journal of Geophysical Research: Earth Surface*, 120, 983–1008, doi:10.1002/2014JF003418, 2015.
- 105 Weertman, J.: Comparison between measured and theoretical temperature profiles of the Camp Century, Greenland, Borehole, *Journal of Geophysical Research*, 73, 2691–2700, 1968.

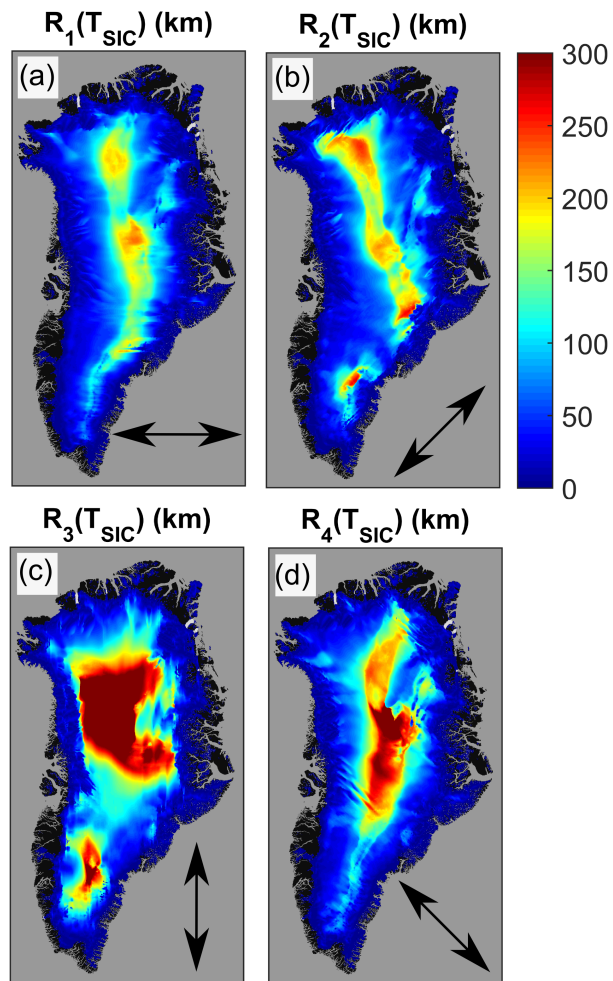


Figure S1. Maps for target window radi vectors using the SICOPOLIS temperature field with $\text{RMS}=1 \text{ dB km}^{-1}$. (a) R_1 , (b) R_2 , (c) R_3 , (d) R_4 . The orientation of each radi vector is shown in each subplot.

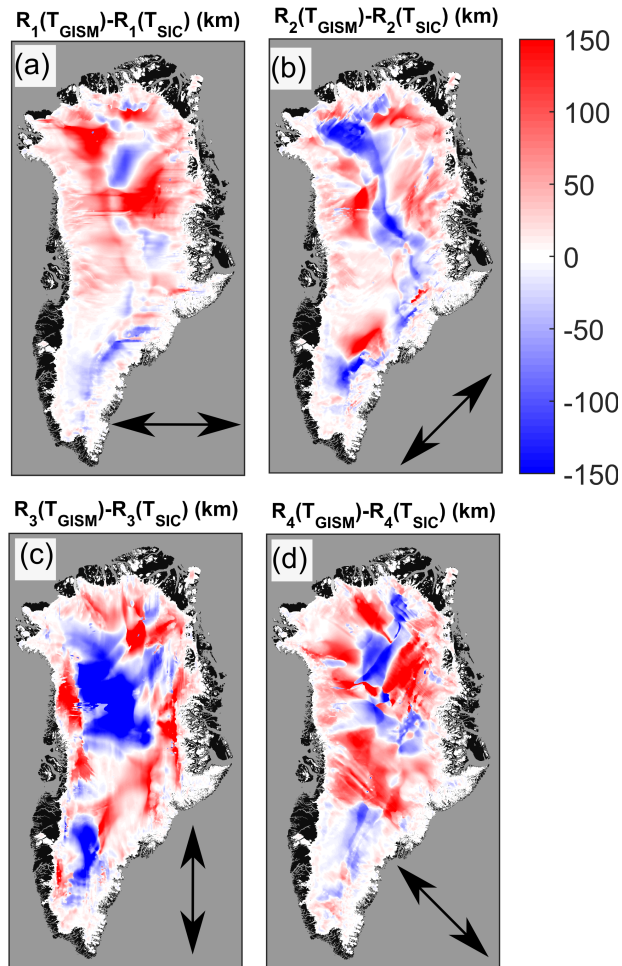


Figure S2. Difference maps for the target window radi vectors with $\text{RMS}=1 \text{ dB km}^{-1}$. **(a)** $R_1(T_{\text{GISM}}) - R_1(T_{\text{SIC}})$, **(b)** $R_2(T_{\text{GISM}}) - R_2(T_{\text{SIC}})$, **(c)** $R_3(T_{\text{GISM}}) - R_3(T_{\text{SIC}})$, **(d)** $R_4(T_{\text{GISM}}) - R_4(T_{\text{SIC}})$. The orientation of each radi vector is shown in each subplot.

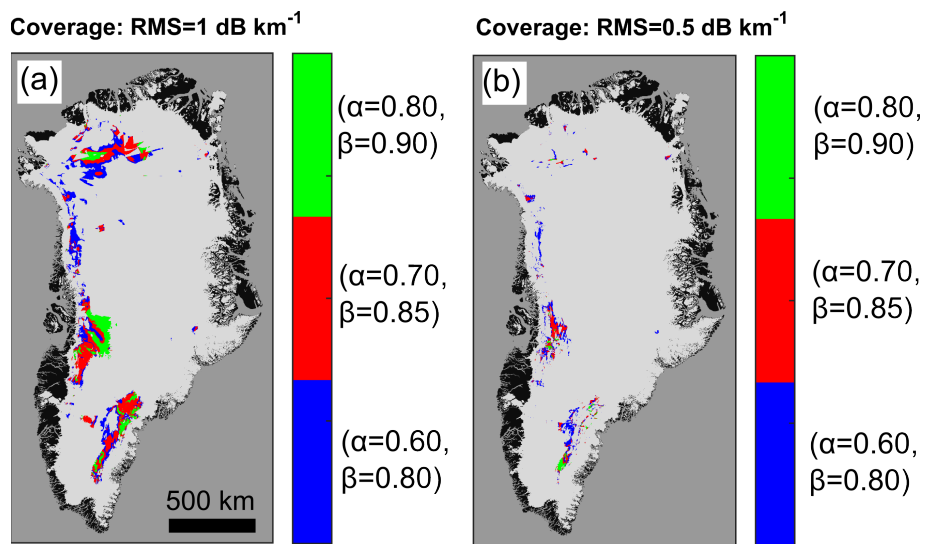


Figure S3. Example of algorithm coverage regions for different window tolerances. (a) RMS=1 dB km¹, (b) RMS=0.5 dB km¹. Both plots are for the 2011 P3 field season data using the GISM temperature field.

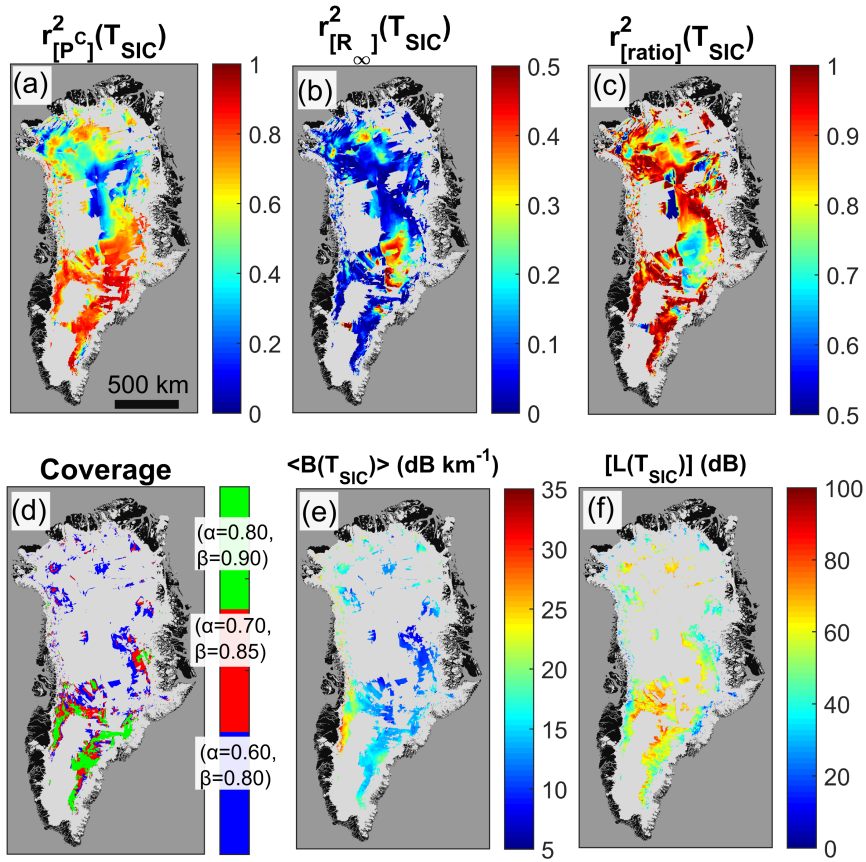


Figure S4. Ice-sheet wide properties of the radar algorithm using the SICOPOLIS temperature field. **(a)** Power-thickness correlation, $r_{[PC]}^2$. **(b)** Arrhenius reflection coefficient-thickness correlation, $r_{[R_{\infty}]}^2$. **(c)** Power ratio-thickness correlation, $r_{[ratio]}^2$. **(d)** Coverage for three thresholds. **(e)** Radar-inferred attenuation rate, $\langle B(T_{SIC}) \rangle$, for $(\alpha, \beta) = (0.60, 0.80)$. **(f)** Radar-inferred attenuation loss, $[L(T_{SIC})]$, for $(\alpha, \beta) = (0.60, 0.80)$.

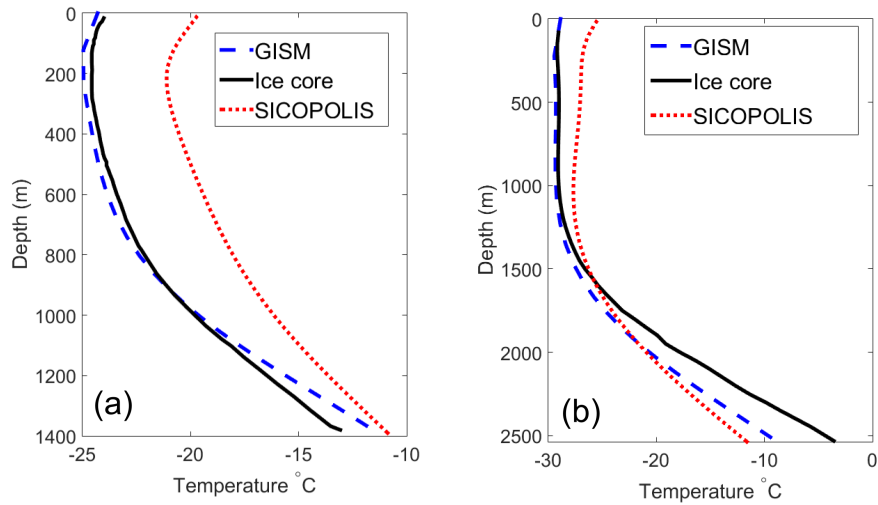


Figure S5. Vertical temperature profiles. (a) Camp Century (Weertman, 1968), (b) NEEM (Macgregor et al., 2015).

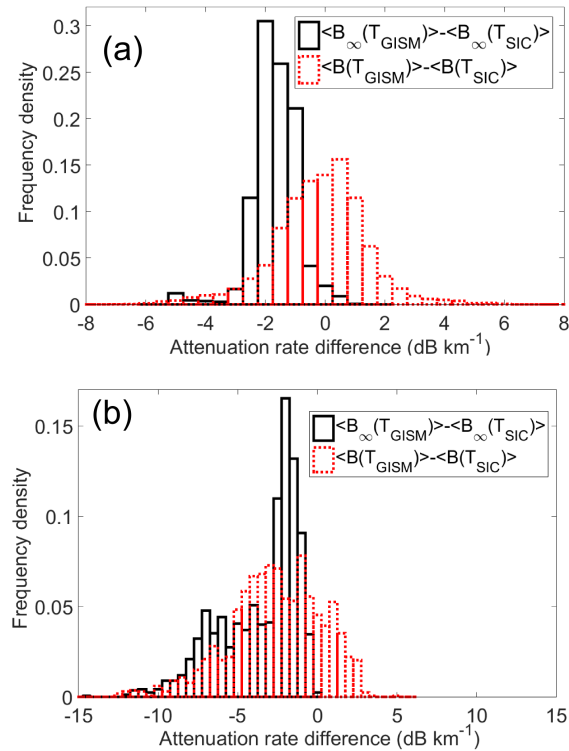


Figure S6. Attenuation rate difference distributions. (a) SW Greenland (drainage basin 6 in Fig. 1), (b) NW Greenland (drainage basin 8 in Fig. 1).

Table S1. Summary of attenuation rate solution variation for independently analysed field season pairs.

Season pair	Algorithm settings	Mean, μ , (dB km ⁻¹)	Standard deviation, σ , (dB km ⁻¹)	Frequency, N.
2012-2011	$T_{\text{GISM}}: (\alpha, \beta)=(0.60, 0.80)$	-0.28	1.34	9869
	$T_{\text{GISM}}: (\alpha, \beta)=(0.70, 0.85)$	-0.11	1.08	5522
	$T_{\text{GISM}}: (\alpha, \beta)=(0.80, 0.90)$	0.26	0.65	953
	$T_{\text{SIC}}: (\alpha, \beta)=(0.60, 0.80)$	-0.71	1.71	6339
	$T_{\text{SIC}}: (\alpha, \beta)=(0.70, 0.85)$	-0.81	1.36	4164
	$T_{\text{SIC}}: (\alpha, \beta)=(0.80, 0.90)$	-0.50	1.01	1371
2013-2011	$T_{\text{GISM}}: (\alpha, \beta)=(0.60, 0.80)$	-0.13	1.46	6698
	$T_{\text{GISM}}: (\alpha, \beta)=(0.70, 0.85)$	-0.26	1.03	3584
	$T_{\text{GISM}}: (\alpha, \beta)=(0.80, 0.90)$	0.181	0.62	521
	$T_{\text{SIC}}: (\alpha, \beta)=(0.60, 0.80)$	-0.73	1.42	5330
	$T_{\text{SIC}}: (\alpha, \beta)=(0.70, 0.85)$	-0.84	1.14	3509
	$T_{\text{SIC}}: (\alpha, \beta)=(0.80, 0.90)$	-1.09	0.85	953
2014-2011	$T_{\text{GISM}}: (\alpha, \beta)=(0.60, 0.80)$	0.05	1.55	10036
	$T_{\text{GISM}}: (\alpha, \beta)=(0.70, 0.85)$	- 0.18	1.12	5045
	$T_{\text{GISM}}: (\alpha, \beta)=(0.80, 0.90)$	0.57	0.85	533
	$T_{\text{SIC}}: (\alpha, \beta)=(0.60, 0.80)$	-0.22	1.48	7934
	$T_{\text{SIC}}: (\alpha, \beta)=(0.70, 0.85)$	-0.38	1.18	5614
	$T_{\text{SIC}}: (\alpha, \beta)=(0.80, 0.90)$	-0.16	1.02	1765
2013-2012	$T_{\text{GISM}}: (\alpha, \beta)=(0.60, 0.80)$	0.33	1.06	6557
	$T_{\text{GISM}}: (\alpha, \beta)=(0.70, 0.85)$	0.33	0.92	4913
	$T_{\text{GISM}}: (\alpha, \beta)=(0.80, 0.90)$	0.38	0.44	343
	$T_{\text{SIC}}: (\alpha, \beta)=(0.60, 0.80)$	0.10	1.02	5272
	$T_{\text{SIC}}: (\alpha, \beta)=(0.70, 0.85)$	0.16	0.85	3319
	$T_{\text{SIC}}: (\alpha, \beta)=(0.80, 0.90)$	0.27	0.59	1202
2014-2012	$T_{\text{GISM}}: (\alpha, \beta)=(0.60, 0.80)$	0.53	1.26	10195
	$T_{\text{GISM}}: (\alpha, \beta)=(0.70, 0.85)$	0.33	0.92	4913
	$T_{\text{GISM}}: (\alpha, \beta)=(0.80, 0.90)$	0.38	0.65	343
	$T_{\text{SIC}}: (\alpha, \beta)=(0.60, 0.80)$	0.32	1.23	7015
	$T_{\text{SIC}}: (\alpha, \beta)=(0.70, 0.85)$	0.35	1.12	4838
	$T_{\text{SIC}}: (\alpha, \beta)=(0.80, 0.90)$	0.32	1.23	586
2014-2013	$T_{\text{GISM}}: (\alpha, \beta)=(0.60, 0.80)$	0.02	0.98	6350
	$T_{\text{GISM}}: (\alpha, \beta)=(0.70, 0.85)$	0.11	0.59	3952
	$T_{\text{GISM}}: (\alpha, \beta)=(0.80, 0.90)$	-0.03	0.32	540
	$T_{\text{SIC}}: (\alpha, \beta)=(0.60, 0.80)$	0.25	1.00	5371
	$T_{\text{SIC}}: (\alpha, \beta)=(0.70, 0.85)$,	0.21	0.79	3889
	$T_{\text{SIC}}: (\alpha, \beta)=(0.80, 0.90)$,	0.40	0.32	1353

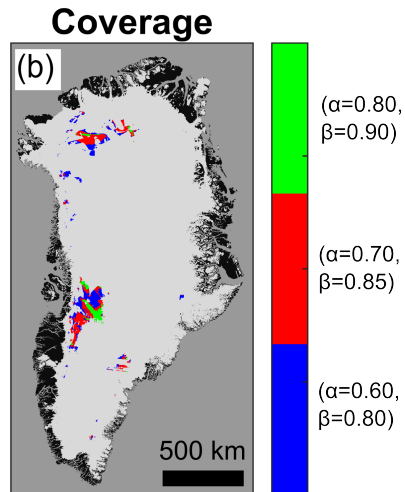
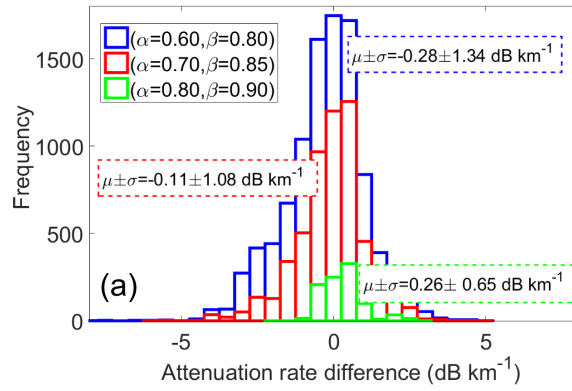


Figure S7. (a) Example of attenuation rate difference distributions for independently analysed field seasons (2012 P3-2011 P3). (b) Coverage overlap region.